Patient-specific electromechanical models of the heart for the prediction of pacing acute effects in CRT: A preliminary clinical validation

M. Sermesant [a,b,*], R. Chabiniok [c], P. Chinchapatnam [b], T. Mansi [a], F. Billet [a], P. Moireau [c], J.M. Peyrat [a], K. Wong [a], J. Relan [a], K. Rhode [b], M. Ginks [b], P. Lambiase [e], H. Delingette [a], M. Sorine [f], C.A. Rinaldi [d], D. Chapelle [c], R. Razavi [b], N. Ayache [a]

[a] INRIA, Asclepios Project, 2004 route des Lucioles, 06 902 Sophia Antipolis, France
[b] King's College London, Division of Imaging Sciences, St. Thomas' Hospital, London, UK
[c] INRIA, Macs Project, Rocquencourt, Le Chesnay, France
[d] Department of Cardiology, St. Thomas' Hospital, London, UK
[e] Heart Hospital, University College London NHS Foundation Trust, London, UK
[f] INRIA, Sisyphe Project, Rocquencourt, Le Chesnay, France

ARTICLE INFO

ABSTRACT

Cardiac resynchronisation therapy (CRT) is an effective treatment for patients with congestive heart failure and a wide QRS complex. However, up to 30% of patients are non-responders to therapy in terms of exercise capacity or left ventricular reverse remodelling. A number of controversies still remain surrounding patient selection, targeted lead implantation and optimisation of this important treatment. The development of biophysical models to predict the response to CRT represents a potential strategy to address these issues. In this article, we present how the personalisation of an electromechanical model of the myocardium can predict the acute haemodynamic changes associated with CRT. In order to introduce such an approach as a clinical application, we needed to design models that can be individualised from images and electrophysiological mapping of the left ventricle. In this paper the personalisation of the anatomy, the electrophysiology, the kinematics and the mechanics are described. The acute effects of pacing on pressure development were predicted with the *in silico* model for several pacing conditions on two patients, achieving good agreement with invasive haemodynamic measurements: the mean error on dP/dt_{max} is 47.5 ± 35 mm Hg s^{-1}, less than 5% error. These promising results demonstrate the potential of physiological models personalised from images and electrophysiology signals to improve patient selection and plan CRT.

© 2011 Elsevier B.V. All rights reserved.

1. Introduction

Cardiovascular diseases (CVD) remain a major cause of morbidity and mortality in the Western World.[1] Within CVD, congestive heart failure (CHF) has an increasing prevalence mainly caused by the steadily increasing number of survivors following myocardial infarction. This leads to progressive derangements in myocardial function arising from scar formation post infarction. CHF has an extremely poor prognosis with a 50% mortality in the first three years after diagnosis. Many patients with heart failure also have significant conduction disease with a broad QRS on ECG often manifested as left bundle branch block. This results in electrical and

mechanical dyssynchrony and declining myocardial pump function. Cardiac resynchronization therapy (CRT) consists of implanting pacing leads to improve the synchronisation of cardiac contraction (Cazeau et al., 2001). Recent large randomised controlled clinical trials have shown that CRT induces significant reductions in morbidity and mortality (Cleland et al., 2005). However, clinical trials have also demonstrated that up to 30% of patients are non-responders to the therapy (Ismail and Makaryus, 2010). There is still significant controversy surrounding patient selection and optimisation of CRT (e.g. lead positioning, pacemaker settings). Current guidelines for selection for CRT rely on symptomatic, echocardiographic and electrocardiographic criteria. A broad QRS (>130 ms) is generally required to merit CRT implant. For instance, recent studies in patient selection showed that patients with heart failure and narrow QRS intervals do not currently benefit from CRT (Beshai et al., 2007) and that no single echocardiographic measure of dyssynchrony may be recommended to improve patient selection (Chung et al., 2008). While image-based methods may give some insights into

who might respond to therapy (Aggarwal et al., 2009), with e.g. detailed strain analysis from Magnetic Resonance Imaging (MRI) (Kirn et al., 2008), the precise prediction of the therapeutic effects and and how best to optimise pacing parameters remain out of reach. Therefore, new approaches are needed in order to provide a more accurate characterisation of ventricular electromechanical function to facilitate improved planning and delivery of the therapy.

In parallel, the last decades have seen major progress in medical imaging, cardiac modelling and computational power facilitating personalised simulations (i.e. using models with patient-specific parameters) of cardiac activity. While the scientific importance and enormous clinical potential of this approach have been acknowledged (Crampin et al., 2004; Hunter and Nielsen, 2005; Kerckhoffs et al., 2008c), its translation into clinical applications has yet to be achieved. We aim to build on the major scientific advances in cardiac modelling that have already been made, in order to proceed to the next level and individualise such models to each specific patient using state-of-the-art multi-modal imaging. This approach has the potential to have a major impact on clinical practice. Indeed, patient management may be improved by allowing the clinical response at specific pacing sites to be predicted and fine-tuned in each patient.

In this article, we demonstrate the necessary first steps and a preliminary validation of the personalisation of an electromechanical model of the heart to predict the response in pressure development due to pacing of the left ventricle at different endo and epicardial sites (see Fig. 1). Such predictions may be used to quantify the improvement in cardiac function that can be expected from CRT. Such a model may also be able to predict the optimal location of the pacemaker leads (stimulation electrodes) and allow optimal programming of timing of the electrical stimulation to ensure a maximal haemodynamic benefit. In this work we have only focused on the acute haemodynamic effects of CRT. The prediction of chronic reverse remodelling of the heart with CRT (Sutton and Keane, 2007) is out of the scope of the presented work.

There is an important body of literature on the functional imaging of the heart, for instance: measurements of electrical activity, deformation, flows, fibre orientation, and on the modelling of the electrical and mechanical activity of the heart. Many of these models are *direct* computational models, designed to simulate in a realistic manner the cardiac action in a realistic manner, often requiring high computational costs and the manual tuning of a very large number of parameters.

Mechanical modelling was used in order to constrain and regularise (Yan et al., 2007) or better interpret deformation from imaging data (Liu and Shi, 2007) with simultaneous parameter estimation (Hu et al., 2003), but without any prediction of changes with therapy.

Recently, computational models have been used to simulate CRT on a generic anatomy in computer studies (Kerckhoffs et al., 2010) or in comparison with animal experiments (Kerckhoffs et al., 2008a; Kerckhoffs et al., 2008b) and have provided important insights on the pathophysiology of dyssynchrony. In order to translate such models into the clinical arena and impact patient management and therapeutic planning, the models need to be individualised to each specific patient, which remains a challenging task especially due to the dimensionality of the problem and the parameter observability.

The proposed approach involves models whose complexity is directly related to the phenomena observed in clinical data. This is the reason why these models are often simplified compared to those published in the literature. The observability of patient parameters parameters (electrophysiological, mechanical and haemodynamic) was crucial in the personalisation step. Utilising a limited number of pre-specified parameters allowed their identification from clinical measurements on a specific patient by solving a tractable *inverse* problem (see Fig. 1). While some steps of this method were interactive, the chosen models have the correct theoretical properties to make an automated adjustment possible.

A preliminary section details the clinical context, the data acquisition, and the data fusion into the same spatio-temporal reference frame. We then present the four sections describing the personalisation of the model anatomy, electrophysiology, kinematics and mechanics. Finally we demonstrate the predictions of acute haemodynamics in comparison to direct interventional measurements for multiple pacing conditions in two clinical cases.

2. Clinical context, data acquisition and fusion

The construction, testing and personalisation of biophysical models rely on the ability to fuse data from an array of sources. For cardiac modelling, the fusion of anatomical, mechanical, and electrophysiological data is of primary importance. This fusion must be both in the spatial and temporal domains. The sources
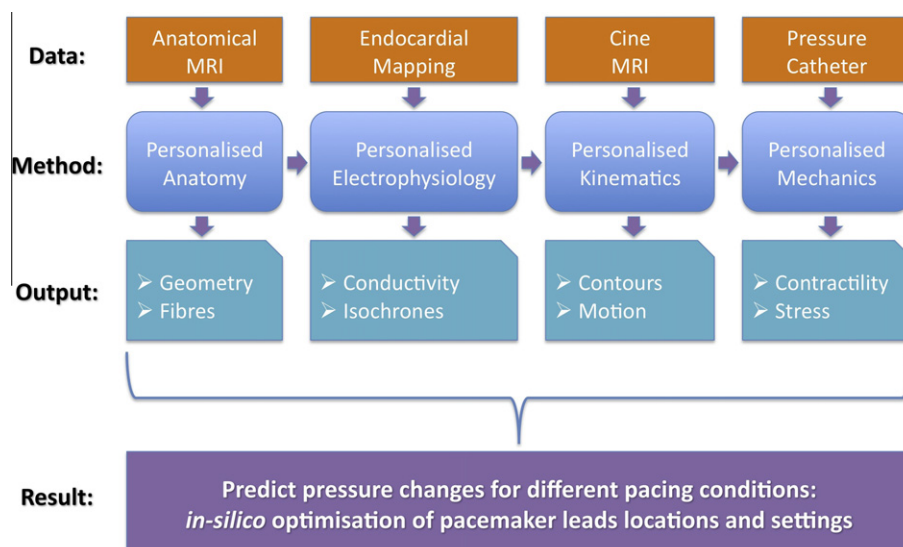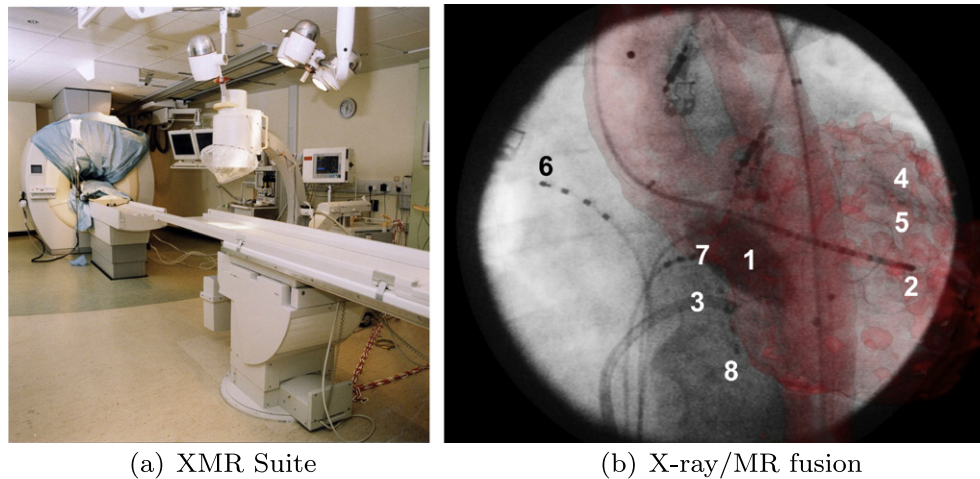

Data:	Anatomical MRI	Endocardial Mapping	Cine MRI	Pressure Catheter
Method:	Personalised Anatomy	Personalised Electrophysiology	Personalised Kinematics	Personalised Mechanics
Output:	➢ Geometry ➢ Fibres	➢ Conductivity ➢ Isochrones	➢ Contours ➢ Motion	➢ Contractility ➢ Stress

Result: Predict pressure changes for different pacing conditions: *in-silico* optimisation of pacemaker leads locations and settings

Fig. 1. Global scheme of the clinical data used for the personalised models, the generated output maps and parameters, and the resulting predictions.

(a) XMR Suite   (b) X-ray/MR fusion

Fig. 2. (a) XMR suite with the MR scanner and the X-ray C-arm. (b) Real-time overlay of MRI-derived left ventricular (LV) surface model (red) onto live X-ray fluoroscopy image (grey scale) to guide the placement of catheters: (1) St. Jude Ensite balloon, (2) LV roving, (3) coronary sinus sheath, (4) coronary venous/epicardial, (5) pressure, (6) high right atrium, (7) His bundle, (8) right ventricle. (For interpretation of the references to colour in this figure legend, the reader is referred to the web version of this article.)
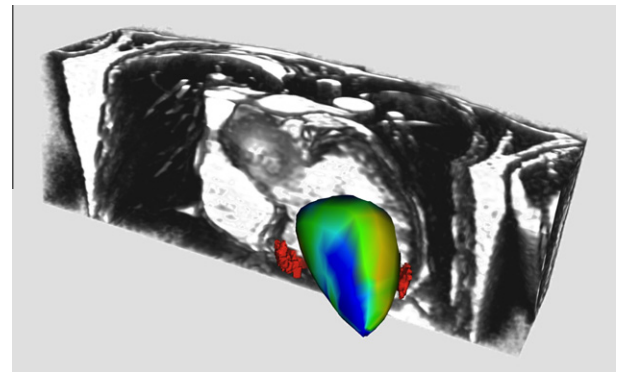
of data used in the presented work are Magnetic Resonance Imaging (MRI), electrophysiology catheters, pressure catheter and X-ray fluoroscopy.

High quality cardiac anatomical and functional data can be obtained from MRI, such as myocardial shape, wall motion, blood flow and infarct sites, with a spatial resolution of approximately $1.5 \times 1.5 \times 7 \, \text{mm}^3$ and a temporal resolution of around 30 ms. Electro-anatomical data can be obtained from catheter-based measurements that are guided using X-ray fluoroscopy with a spatial resolution of less than a centimetre and a temporal resolution close to a millisecond. Acute haemodynamic data is acquired using a high fidelity (200 Hz) pressure sensor to measure left ventricular pressure.

Spatial fusion of electrical and anatomical data requires an effective image registration strategy. Our solution has focused on the use of an X-ray/MR (XMR) hybrid imaging system that allows the seamless collection of both MRI and X-ray-based data (see Fig. 2). We have developed a real-time registration solution (Rhode et al., 2005) that allows the spatial integration of MRI-based anatomical and functional data with X-ray-based catheter data, such as intracardiac electrophysiological and pressure signals. For the temporal integration, the electrocardiogram provides the information on the heart rhythm to enable the synchronisation of the datasets.

We present data based on two clinical cases scheduled to receive CRT. The first patient was a sixty year old woman with heart failure and NYHA class III symptoms.[2] The aetiology of heart failure was non-ischaemic dilated cardiomyopathy with no flow-limiting disease on coronary angiography although cardiac MRI did show subendocardial postero-lateral scar in the left ventricle. The left ventricular ejection fraction was 25% on maximal tolerated heart failure medication. The surface ECG demonstrated significant conduction disease with left bundle branch block (LBBB) QRS duration of 154 ms (normal QRS is less than 120 ms). Echocardiography, including Tissue Doppler, confirmed significant mechanical dysynchrony in keeping with the ECG findings.

The second patient was a seventy-seven year old woman with a much more developed dilated cardiomyopathy. She was in NYHA class III heart failure with a LV ejection fraction of 18% and left

Fig. 3. Fusion of late-enhancement derived scars (red surfaces), anatomical MR (volume rendering) and Ensite isochronal map (coloured surface). (For interpretation of the references to colour in this figure legend, the reader is referred to the web version of this article.)
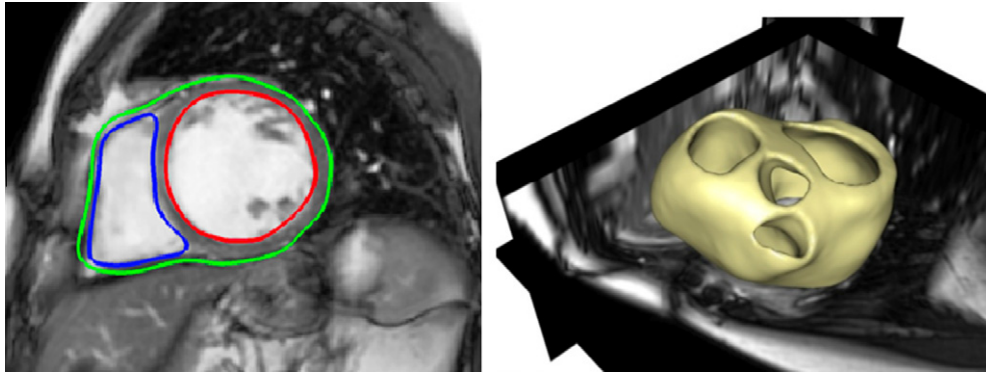
bundle branch block QRS duration of 200 ms. There was no late gadolinium enhancement but functional conduction block was observed in the electrophysiological mapping.

For both cases, the clinical data used to set up the patient-specific models consisted of a cine-MRI[3] for the estimation of ventricular function and volumes and late enhancement images with gadolinium contrast agent for scar anatomy (in case of scars). A non-contact mapping study was performed using the Ensite 3000 multi-electrode array catheter system (St Jude, Sylmar, CA). This consists of a 64 laser-etched wire braid mounted on an 8 mm balloon. The array records intracavity far-field potentials that are sampled at 1.2 kHz and digitally filtered at 0.1–300 Hz. The resulting signals allow the reconstruction of over 3000 virtual unipolar electrograms superimposed on a computerised model of the left ventricle created using a locator signal on a roving endocardial catheter. We can then obtain both isopotential and isochronal maps. While non-contact mapping can suffer from motion and distance artefacts, it is well suited to create biophysical models as it can map several different pacing conditions from a single heart beat (while contact mapping would require a relatively large number of cycles for each pacing mode). The XMR fusion provides the location of the Ensite
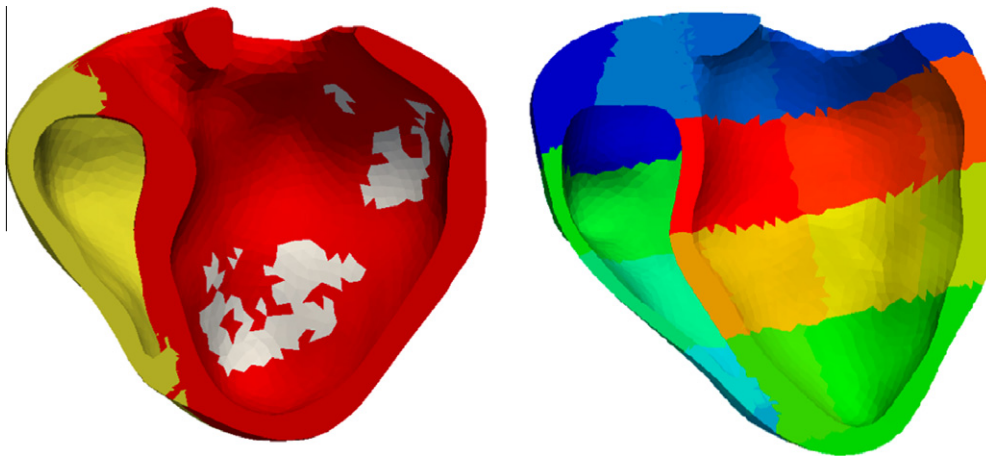
---

[2] NYHA classes stand for the stages of heart failure according to the New York Heart Association. Patients with NYHA III are comfortable at rest but any other activity causes fatigue, palpitation, or dyspnea.

[3] cine-MRI usually cover the ventricles by a set of 2D dynamic sequences for which the image data are acquired with a temporal resolution of 20–40 ms.

Fig. 4. Personalised anatomy using image segmentation. Left: Three surfaces were defined during the segmentation, the left ventricular endocardium (in red), the right ventricular endocardium (in blue) and the epicardium (in green). Right: 3D visualisation of the obtained anatomical model. (For interpretation of the references to colour in this figure legend, the reader is referred to the web version of this article.)

Fig. 5. Labelled volumetric mesh. Three main areas are defined: left ventricle (in red), right ventricle (in yellow) and scar (in white). Additional AHA segments subdivision is also performed for regional personalisation. (For interpretation of the references to colour in this figure legend, the reader is referred to the web version of this article.)

mapping with respect to the MR-derived information (see Fig. 3). We will illustrate the whole method with the data from Patient 1, but the same process was applied to the data from Patient 2.

3. Personalised anatomy

3.1. Model specification

The anatomical model used is the compact (i.e. without trabeculae) ventricular myocardium. As we did not simulate the valves, we did not integrate the papillary muscles into the segmentation. This anatomical model is represented with a tetrahedral mesh which resolution is around 2 mm (mean edge length). This is to be compatible with the resolution of the data and the computational time of the models. We label the different tetrahedra of the mesh for regional parameter adjustment. The labels used include the AHA segments and the scars. Endocardial and epicardial surfaces were labelled as well. The complex cardiac fibre architecture has an important role in the electrical and mechanical function of the heart: electrical propagation and mechanical contraction are mainly along the fibre direction. The introduction of the fibre orientation in cardiac electromechanical modelling is thus essential for accurately simulating cardiac function. We use a synthetic model built with analytical laws describing general trends of fibre orientations observed in different studies (Streeter, 1979). We assign a fibre orientation to each vertex of the mesh.
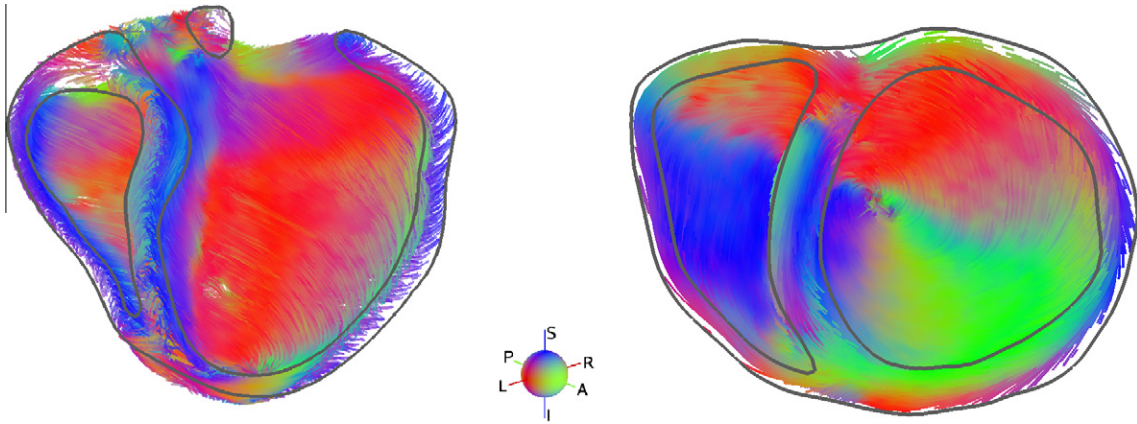
3.2. Model personalisation

There is an extensive literature on the segmentation of the heart from medical images (see for instance (Ecabert et al., 2008; Zheng et al., 2008; Peters et al., 2010) and references therein). However, to cope with extreme and variable anatomies due to pathologies, we developed a simple yet efficient semi-automatic method which combines specific image processing tools to extract the biventricular myocardium from cine-MRI. We segmented in the mid-diastolic volume of the cardiac sequence: the left ventricle (LV) endocardium (Fig. 4, red contour), the right ventricle (RV) endocardium (Fig. 4, blue contour) and the epicardium (Fig. 4, green contour). To this aim, we developed an interactive tool based on variational implicit functions (Turk and O'Brien, 1999). This tool[4] allows the user to intuitively model any 3D surface in the 3D scene by placing, moving or deleting control points inside, on and outside the desired surface (Toussaint et al., 2008). Then it computes in real-time the implicit function that interpolates those points and extracts its zero-level set surface. Union and intersection operations using these surfaces enables to generate a binary mask of the patient myocardium muscle.

Then the CGAL[5] and GHS3D[6] software were used to respectively extract the surface mesh from the volumetric binary mask and build
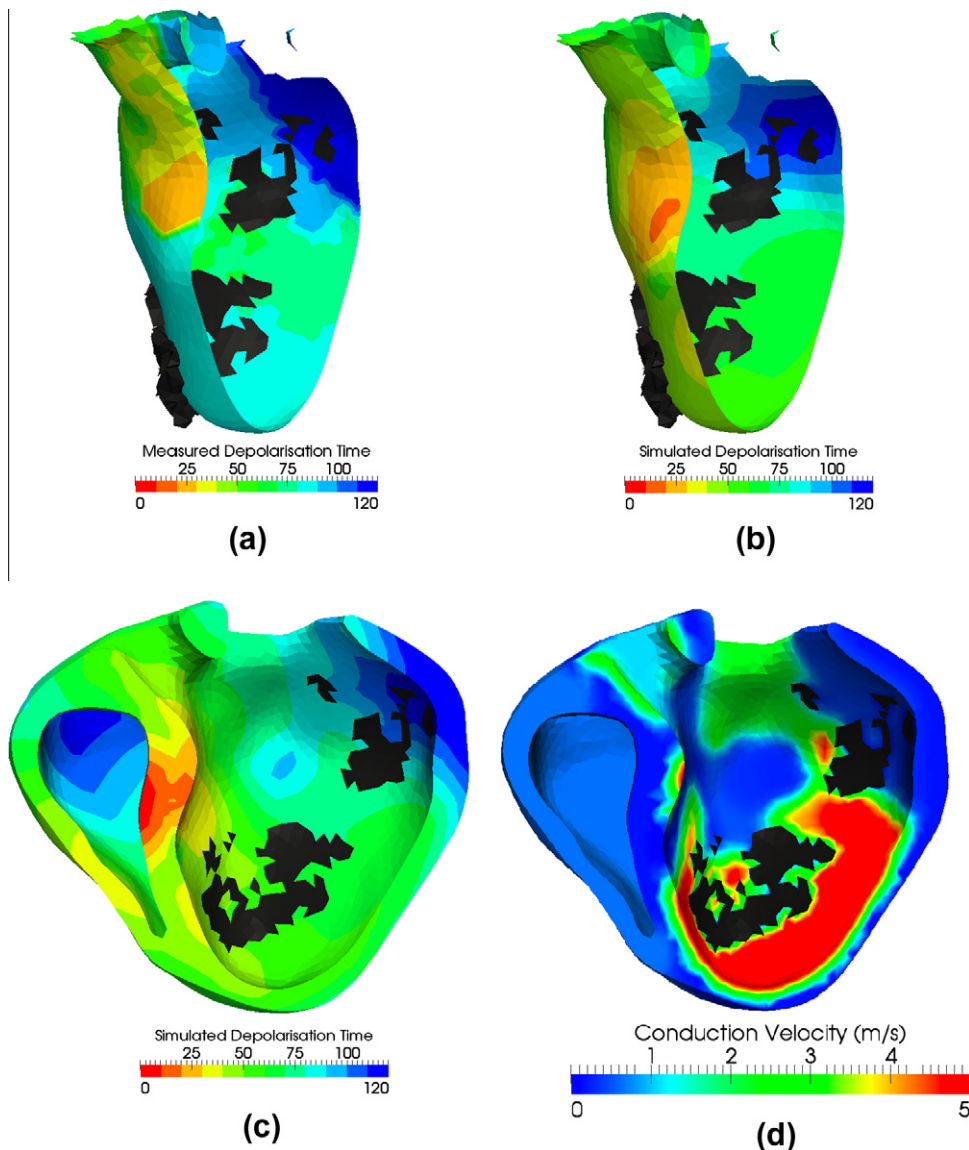
---

[4] http://www-sop.inria.fr/asclepios/software/CardioViz3D/.
[5] http://www.cgal.org/.
[6] http://www-roc.inria.fr/gamma/gamma/ghs3d/.

Fig. 6. Long axis and short axis cut of the fibre orientations generated on the patient anatomy according to the statistical atlas information. Colour encodes direction. (For interpretation of the references to colour in this figure legend, the reader is referred to the web version of this article.)

Fig. 7. (a) Long axis cut of the measured isochrones projected on the MR-derived endocardium (septum is in front). (b) Simulated endocardial isochrones with the personalised model, and (c) within the whole myocardium. (d) Conduction velocity (CV) parameter map from the automatically estimated AC. High CV areas (in red) represent probable areas of Purkinje extremities. Black regions are scar locations from MRI. (For interpretation of the references to colour in this figure legend, the reader is referred to the web version of this article.)

the volumetric tetrahedral anatomical model from the surface mesh. Each tetrahedron was automatically labelled according to the anatomical region it belonged to (LV, RV or scar tissue, see Fig. 5). The scar label was based on the expert manual delineation on late enhancement MRI. Also, for regional parameter estimation, subdivision of the left ventricle according to the American Heart Association 17 segments was performed, see Fig. 5.

We generate the personalised fibre orientations by setting the parameters of the analytical model according to the angles observed in a statistical atlas (Peyrat et al., 2007), mapped into the geometry of the patient's heart (see Fig. 6). We only used here transverse anisotropy, neglecting the effect of the myocyte layers (Caldwell et al., 2009).

3.3. Error analysis

From visual inspection, the manual segmentation error is close to the image resolution. We can add more control points to refine the mesh, but the uncertainty on the data due to the large slice thickness and differences in breathing position make it unnecessary.

There is definitely error in the personalised fibres as we do not have patient data to guide this personalisation and we do not model the influence of the pathology on these.

4. Personalised electrophysiology

4.1. Model specification

Modelling cellular electrophysiology (EP) is a very active research area (Hodgkin and Huxley, 1952; Noble, 1962; Beeler and Reuter, 1977; Luo and Rudy, 1991; Noble et al., 1998; TenTusscher et al., 2004). At the organ level, it involves a cell membrane model embedded into a set of partial differential equations (PDEs) representing a continuum. Solving the dynamic PDEs is computationally very demanding, due to the space scale of the electrical propagation front being much smaller than the size of the ventricles, and the stability issues related to the dynamic nature of the equations. Moreover, the currently available clinical electrophysiological data only reliably measures the depolarisation times, and not the extracellular or transmembrane potentials. The advantage of the Eikonal equation (Keener and Sneyd, 1998; ColliFranzone et al., 1990) is that the front can be observed at a larger scale, resulting in much faster computations. Furthermore this equation can be solved very efficiently by using an anisotropic multi-front fast marching method (Sermesant et al., 2007). For these reasons, we based our model on the Eikonal diffusion (ED) equation. The static ED equation for the depolarisation time (T_d) in the myocardium is given by

$$c_0\sqrt{\nabla T_d^t D\nabla T_d} - \nabla \cdot (D\nabla T_d) = \tau \qquad (1)$$

where c_0 is a dimensionless constant related to the cell membrane, τ is the cell membrane time constant, ∇ the gradient operator and $\nabla\cdot$ the divergence operator. The tensor quantity relating to the fibre directions is given by $D = dA\bar{D}A^t$, where d is the square of the membrane space constant and thus related to the volumetric electrical conductivity of the tissue, A is the matrix defining the fibre directions in the global coordinates system and $\bar{D} = \text{diag}(1,\lambda^2,\lambda^2)$. The parameter λ is the anisotropic ratio of membrane space constants along and transverse to the fibre direction f and is of the order 0.4 in human myocardium (see (Tomlinson, 2000) for more details on the ED equation and its parameters). $CV = c_0\sqrt{d}/\tau$ is homogeneous to a conduction velocity thus we present this parameter in the parameter map (Fig. 7) for easier interpretation.
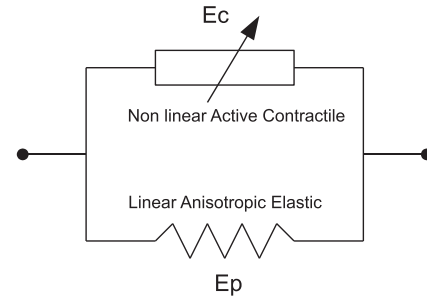

Fig. 8. Simplified model constitutive law with a linear anisotropic elastic element (E_c) and a non-linear active contractile element (E_c).

4.2. Model personalisation

To personalise the electrophysiological model, there were two important adjustments to perform: the onset of the electrical propagation, and the local conduction velocity. From the Ensite map of the left ventricular endocardium, we could see where the right ventricle excitation traverses the septum into the left ventricle (it corresponds to the isochrone 0 in the mapping data). We thus estimated the right ventricle Purkinje extremities as the symmetric through the septum of the zero-isochrone in the left ventricle Ensite data. We then used the ECG to compute the QRS duration in order to estimate a mean conduction velocity. We finally estimated the cardiac cell parameter d in the Eikonal model which corresponds to an apparent conductivity (AC). We estimated the AC by matching the simulated propagation times of the model to the clinically measured propagation times of the patient (see Fig. 7).

Several methods for the automatic adjustment of the AC were already proposed for surfaces (Moreau-Villéger et al., 2006; Chinchapatnam et al., 2008). Such approaches were extended to volumetric models, by using a coupled error criterion both on endocardial depolarisation times (Fig. 7a) and QRS duration. The multidimensional iterative minimisation is done using the NEWUOA algorithm (Powell, 2006).

The AC estimation was divided into two parts, first the endocardium and then the myocardial wall. This adjustment has the following steps:

1. Location of the electrical onset from the mapping data.
2. Estimation of the endocardial regional AC by minimising the regional mean error between measured and simulated depolarisation times on the endocardial surface, with adaptive domain decomposition (at each iteration, we subdivide the region with the highest error, see (Chinchapatnam et al., 2008) for details).
3. Coupled estimation of the myocardial AC. The LV myocardium is divided into four regions: Septal, Anterior, Lateral, Posterior. For each region, a single AC value is used for the whole myocardial wall thickness (except the endocardium). We compute this estimation by minimising a cost function J composed of both the endocardial error with mapping and the QRS duration error with ECG:

$$J = \sum_{j=1}^{n_e}\frac{1}{n_e}\left(T_j^s - T_j^m\right)^2 + \left(T_{onset}^s - T_{onset}^m\right)^2 + (QRS^s - QRS^m)^2$$

where T_d^s and T_d^m are the simulated and measured endocardial depolarisation times on the n_e endocardial points, T_{onset}^s and T_{onset}^m are the simulated and measured onset depolarisation times on LV endo, and QRS^s and QRS^m the simulated and measured QRS durations.

4.3. Error analysis

We applied this method to the baseline measurements and obtained a good fit to the data (Fig. 7b), with a final mean error

Table 1
Patient 1 final error values obtained after electrophysiology model personalisation (SD: standard deviation).

Pacing mode	Mean error ± SD (ms)	QRS error (ms)
Baseline	9.1 ± 7.3	1.3
Atrial	7.3 ± 6.9	1.6
RV	7.3 ± 6.5	0.1
LV endo	6.0 ± 5.5	0.4
TriV	9.1 ± 6.5	5.2

Table 2
Patient 2 final error values obtained after electrophysiology model personalisation (SD: standard deviation).

Pacing mode	Mean error ± SD (ms)	QRS error (ms)
Baseline	8.0 ± 7.1	0.065
Atrial	7.5 ± 7.0	0.054
RV	8.7 ± 8.1	0.11
BiV	11.6 ± 10.3	2.8
TriV	8.1 ± 8.5	2.4

Table 3
Mechanical parameter values used in the two cases after personalisation. We can observe the increased stiffness and decreased contractility of the scars in Patient 1 and the generally increased stiffness and decreased contractility in Patient 2, that may be due to the importance of the cardiomyopathy.

Parameter		Patient 1	Patient 2
Hyperelasticity	κ_1 (in Pa)	Non-scarred: 10^4	1.5×10^4
		Scar: 10^5	
Hyperelasticity	κ_2 (in Pa)	Non-scarred: 80	120
		Scar: 800	
Hyperelasticity	κ (in Pa)	Non-scarred: 10^5	1.5×10^6
		Scar: 10^6	
Peak contractility	σ_0 (in Pa)	LV: 3.4×10^5	3.0×10^5
		RV: 1.7×10^5	1.5×10^5
		Scar: 4.6×10^4	
Proximal capacitance	C_p (in m^3/Pa)	2.3×10^{-10}	7.0×10^{-10}
Proximal resistance	R_P (in Pa s/m^3)	2.1×10^7	7.2×10^6
Distal capacitance	C_d (in m^3/Pa)	7.2×10^{-9}	2.7×10^{-8}
Distal resistance	R_d (in Pa s/m^3)	2×10^8	8×10^7

between simulated and measured isochrones of 9.1 ms. Fig. 7c shows the CV map from the estimated AC. The scar locations were obtained from the segmentation of the late enhancement MR images. The resulting AC map provides information on some potential Purkinje network (high values) as well.

In the second patient case, a site of functional block was identified in the mapping data isochrones, and automatically estimated when fitting the isochrones. We defined it as transmural, as simulations without fully transmural block were not producing results in accordance with the endocardial data. We ran the personalisation algorithm and obtained a 8.0 ms final mean error.

For Patient 1, the final number of endocardial regions was 56, with the smallest region having an area of around 23 mm². For Patient 2, the final number of endocardial regions was 37, with the smallest region having an area of around 75 mm² (see Table 1).

This personalisation provides results with less than 10% error on the endocardium and a realistic extrapolation to the whole myocardium. The detailed figures of the errors for the different pacing conditions are presented in Table 2. These errors are low after each personalisation, however we only have a very partial view of the propagation from baseline data (only the left ventricle endocardium, and for one condition), thus the accurate prediction of the isochrones for different pacings is still work in progress.

In the following two sections we discuss how a simplified model was used to estimate the cardiac motion (kinematics), and then how a more complex model was used to simulate the cardiac forces (mechanics).

5. Personalised kinematics

5.1. Model specification

In this subsection, we extract the cardiac motion from the cine-MRI. There are numerous methods proposed in the literature for this task, but we want here to take advantage of the entire patient data already integrated through the previous two sections. Thus we use a 3D proactive deformable model approach to estimate the motion of the heart from cine-MRI volumes. It enables to input the prior knowledge on the anatomy and electrophysiology in the motion estimation, while other methods from the literature cannot benefit from such knowledge.

The 3D model used here was a simplified electromechanical model designed for cardiac image analysis and simulation (Sermesant et al., 2006a) (see Fig. 8), derived from a multi-scale modelling

of the myocardium (Bestel et al., 2001). The complexity of the model was designed to match the relatively sparse measurements. It is composed of two elements in parallel: one anisotropic linear visco-elastic to represent the passive properties of the tissue and one active contractile element controlled by the command u. This command was set to a constant k_{ATP} (the contraction rate) when depolarisation occurs at time T_d and to a constant $-k_{RS}$ (the relaxation rate) when repolarisation occurs at repolarisation time $T_r = T_d + APD$, with APD a given Action Potential Duration. For one tetrahedral element, the active stress σ_c was controlled by u through the ordinary differential equation (a reduced version of the more detailed stress model used for personalised mechanics in next Section 6):

$$\dot{\sigma}_c + |u|\sigma_c = |u|_+ \sigma_0$$

where σ_0 is the peak stress parameter and $|u|_+$ represents the positive part of the command u (u is positive during contraction and negative during relaxation). Then, the integral of the divergence of the active stress over a tetrahedron results in a 3D force vector $\vec{f_C} = \sigma_c \int_S (\vec{f} \cdot \vec{n}) \vec{f} \, dS$ with f the fibre direction, $\vec{n}$ the surface normal and dS the element surface of the tetrahedron. The simplified dynamics law is then:

$$M\ddot{Y} + C\dot{Y} + KY = F_P + F_C + F_B \qquad (2)$$

with Y the position vector, $\dot{Y} = dY/dt$ the velocity, $\ddot{Y} = d^2Y/dt^2$ the acceleration, K the stiffness matrix for the transverse anisotropic elastic part (parallel element), M a diagonal mass matrix, C the Rayleigh damping matrix (internal viscosity component), F_C the assembled contraction force, F_P the developed pressure forces in the ventricles and F_B a force vector corresponding to the other boundary conditions. Furthermore, we simulated the four cardiac phases (filling, isovolumetric contraction, ejection and isovolumetric relaxation) as detailed in Sermesant et al. (2006a). Finally, the arterial pressures were computed using a Windkessel model (Stergiopulos et al., 1999).

5.2. Model personalisation

We estimated the motion of the heart by coupling this electromechanical model with cine-MRI, based on the proactive deformable model described in Sermesant et al. (2006a), Billet et al. (2009). We have shown in Billet et al. (2008) that this method is related to the data assimilation approach described in Moireau et al. (2008). Numerous studies on the adjustment of a geometrical model of the heart to time series of medical images are based on the concept of deformable models (Park et al., 1996; McInerney

and Terzopoulos, 1996; Montagnat and Delingette, 2005). In this framework, a mesh is fitted to the apparent boundaries of the myocardium by minimising the sum of two energies: a data attachment term and a regularisation term. In our case, this regularisation term consisted in the energy of the dynamical system of the simplified electromechanical model of the heart.

We aimed to minimise the difference between the simulated motion of the myocardium and the apparent motion in the images. To this end, we defined an image force F_I which attracts each surface vertex Y_i towards its corresponding voxel Y_i^{img} in the image. This corresponding voxel is searched for both with a gradient approach (Montagnat and Delingette, 2005) (looking for high gradient voxels along the mesh normal direction) and with a block-matching algorithm (Ourselin et al., 2000) associated with each surface vertex of the mesh. This combination allowed to correct the block-matching tracking, when the initial position was not exactly on the endocardium. The new law of dynamics with these additional image forces F_I is then given by this equation:

$$M\ddot{\widehat{Y}} + C\dot{\widehat{Y}} + K\widehat{Y} = F_P + F_C + F_B + F_I \qquad (3)$$

where $\widehat{Y}$ is the estimated position of the heart nodes.

From global parameters like the ejection fraction we could calibrate the mechanical parameters of the contractile element (k_{ATP}, k_{RS} and σ_0).

5.3. Error analysis

Fig. 9 shows the MR images at end-diastole and at end-systole of the cardiac cycle. The superimposed lines represent the intersection of the endocardial and epicardial surfaces of the mesh with the images.

We can observe that despite the limited quality of routine clinical images, the estimation of the myocardium contours is good, especially for the left ventricle (see Fig. 9 for a comparison with an independant manual delineation, we focus here on the compact myocardium, not on papillary muscles and trabeculae). Due to the lack of contrast on the epicardium and the thinness of the right ventricle, achieving a good tracking of the RV wall is still challenging.
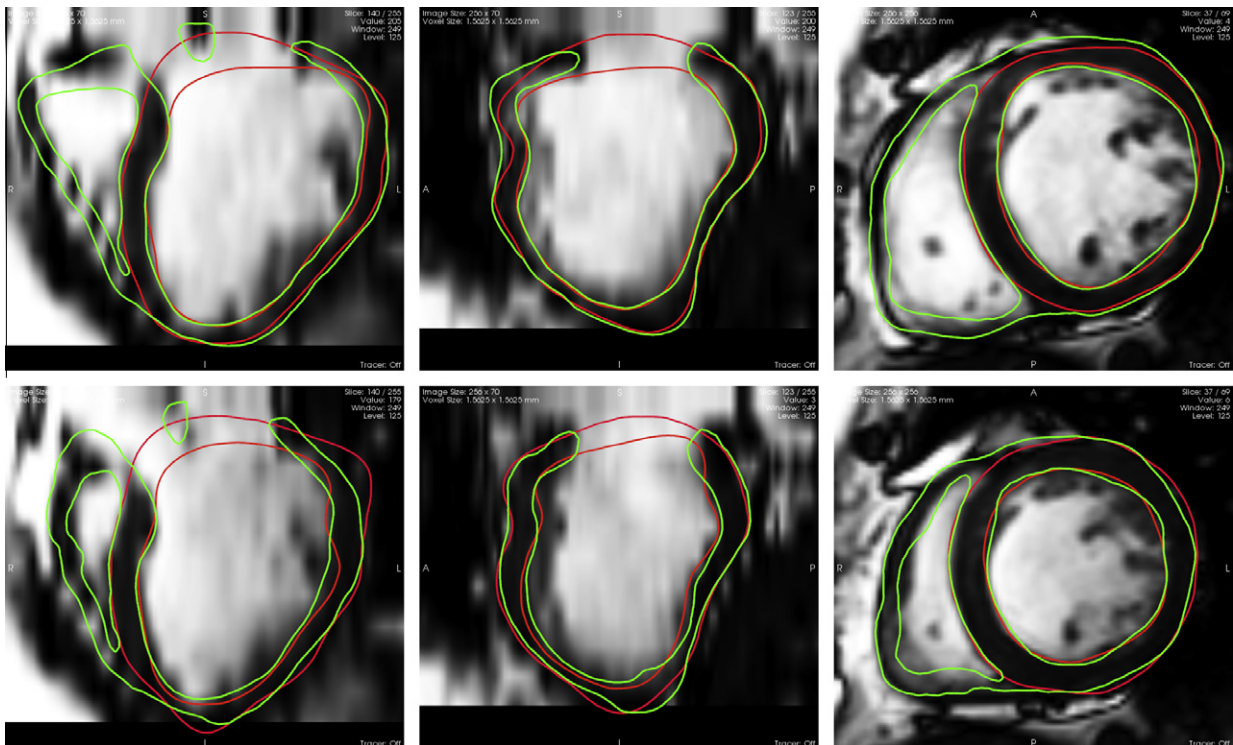
This approach allowed to recover a realistic motion of the heart, including a twisting component captured by the model even if the images provide information mostly in the direction orthogonal to the endocardium. This was actually validated with additional tagged-MRI acquired on the first patient, where the circumferential motion estimated with this method from cine-MRI was in good agreement (up to the image resolution) with the one measured from the tags by manually tracking tag intersections in seven short axis slices (see Fig. 10). A more detailed validation and sensitivity analysis of this method can be found in Wong et al. (2010).

6. Personalised mechanics

We then adjust a more detailed mechanical model in order to personalise the simulated pressure curve.
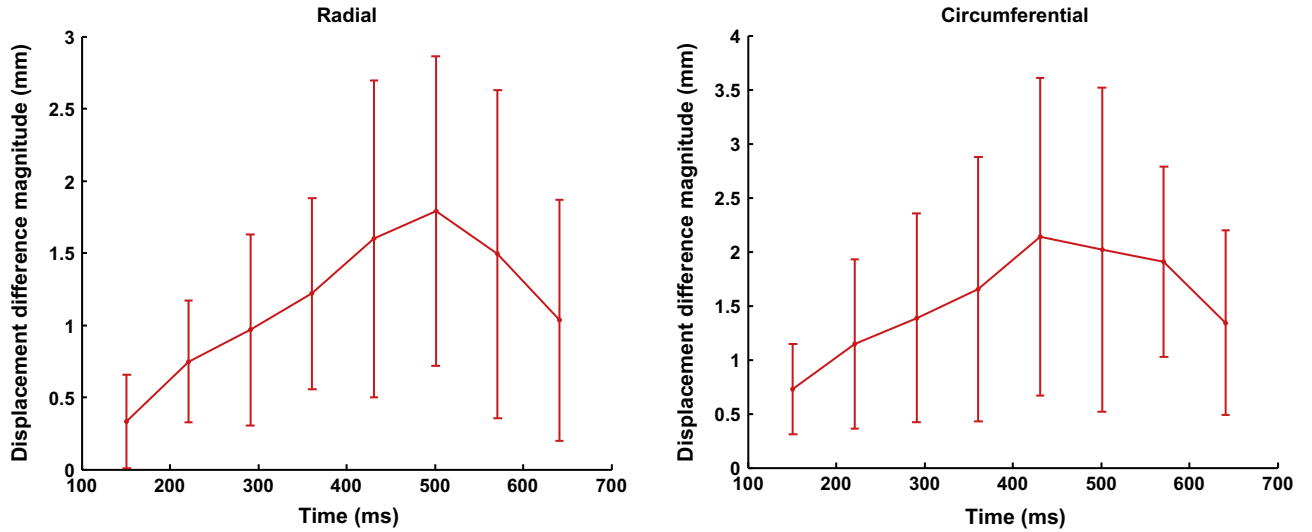
6.1. Model specification

The myocardium constitutive law has to model the active, non-linear, anisotropic, incompressible and visco-elastic properties of the cardiac tissue. Numerous formulations have been proposed in the literature, see e.g. (Humphrey et al., 1990; Nash, 1998; Hunter et al., 1997; Caillerie et al., 2003; Hunter et al., 1998; Smith et al., 2000; Humphrey, 2002; Sachse, 2004) and references therein. The particularity of the model used in this study is that it was designed to have a complexity compatible with the clinical data used for the personalisation. As apparent motion and left ventricular pressure are the main components of the observations, we relied on models

Fig. 9. Results of the motion tracking: manual delineation of LV blood pool and LV epicardium (without valves, red line) estimated myocardial mesh (green line) superimposed with cine-MRI at (top) end-diastole and (bottom) end-systole. (For interpretation of the references to colour in this figure legend, the reader is referred to the web version of this article.)

Radial

Circumferential

Fig. 10. Mean radial (left) and circumferential (right) displacement error between the estimated motion (personalised kinematics) and the manually measured one in seven short axis tagged MRI slices (in-plane image resolution is 1.6 mm^2).

with limited parameters representing the passive and active parts of the constitutive law.

Most of the components of the mechanical model discussed in this section are quite classically used in heart models. However, the specificity of our model are its consistency with essential thermomechanical requirements and the physiological interpretation of its components. Moreover, its global integration preserves these requirements from the continuous dynamical equations to the discrete versions (see details in Sainte-Marie et al., 2006).

Denoting by σ_c the active stress and by e_c the strain along the sarcomere, the myofibre active constitutive law relates σ_c and e_c as follows (Bestel et al., 2001):
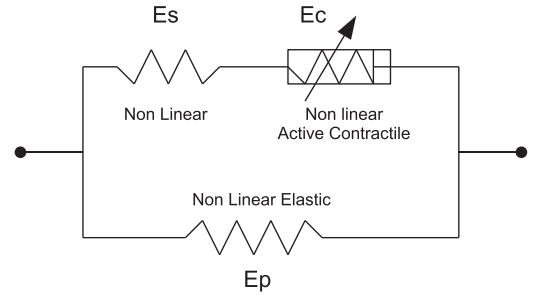
$$\begin{cases} \dot{\tau}_c = k_c \dot{e}_c - (\alpha|\dot{e}_c| + |u|)\tau_c + \sigma_0|u|_+ & \tau_c(0) = 0 \\ \dot{k}_c = -(\alpha|\dot{e}_c| + |u|)k_c + k_0|u|_+ & k_c(0) = 0 \\ \sigma_c = \tau_c + \mu\dot{e}_c + k_c\xi_0 \end{cases} \quad (4)$$

where u still models the electrical input from the action potential ($u > 0$ contraction, $u \leqslant 0$ relaxation). As the previous simplified model was derived from this one, identically named variables and parameters are related but here the active component is more detailed. Parameters k_0 and σ_0 characterise muscular contractility and respectively correspond to the maximum value for the active stiffness k_c and for the stress τ_c in the sarcomere, while μ is a viscosity parameter.

The above active constitutive law was used within a rheological model of Hill-Maxwell type (Chapelle et al., 2001), see Fig. 11 where the component E_c is associated with the above contraction law, while E_s and E_p represent elastic laws. This rheological model is compatible with large displacements and strains and led to a continuum mechanics description of the cardiac tissue (Sainte-Marie et al., 2006). In the parallel branch of the Hill-Maxwell model – namely, for element E_p – we considered a viscoelastic isotropic behaviour, with a hyperelastic potential given by the Ciarlet-Geymonat volumic energy (Le Tallec, 1994):

$$W = \kappa_1(J_1 - 3) + \kappa_2(J_2 - 3) + \kappa(J - 1) - \kappa\ln J, \quad (5)$$

where (J_1, J_2, J) denote the reduced invariants of the Cauchy-Green strain tensor, and $(\kappa_1, \kappa_2, \kappa)$ are material parameters. As regards the branch containing E_c, it relates to a behaviour directed along the cardiac fibres – namely, the corresponding combined stress–strain law is one-dimensional, with that of E_s taken linear. Note that this introduces anisotropy in the overall passive behaviour.
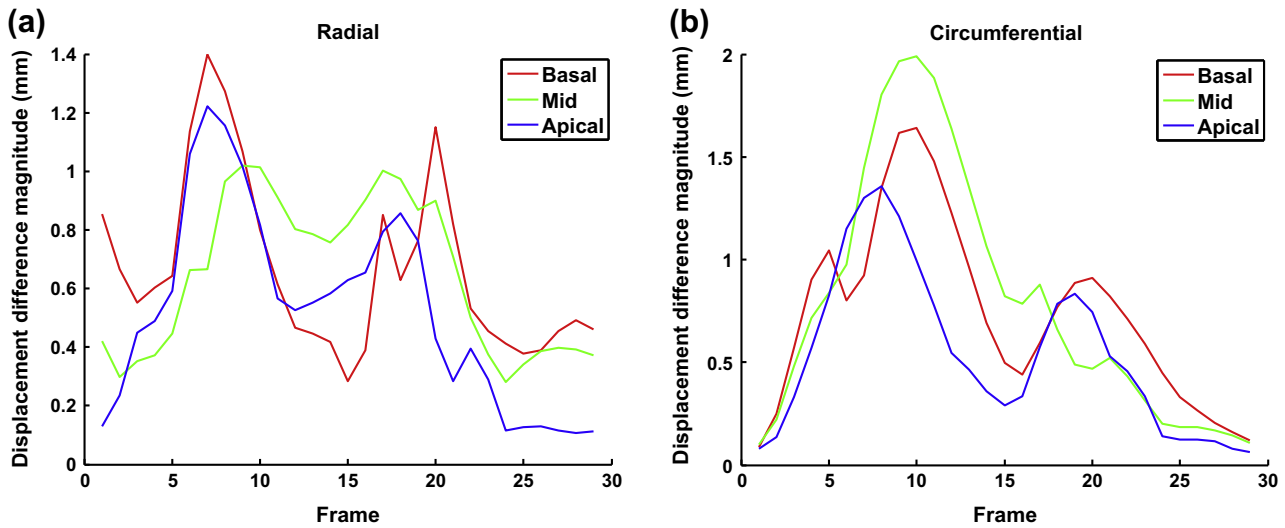

Fig. 11. Complex model constitutive law with a non-linear hyperelastic element (E_p), a non-linear active contractile element (E_c), and a non-linear series element (E_s).

Then the pressure within the ventricle represents the main loading which balances the tissue stresses in the dynamics equilibrium equation, also called principle of virtual work when written in a weak form, see (Sainte-Marie et al., 2006) for the detailed expression in the heart model considered. During the ejection phase, the ventricle pressure also equilibrates the Windkessel pressure. Globally, the model equations are closed, and we can see the ventricle pressure as an output of the system, while the electrical activation u is the input.
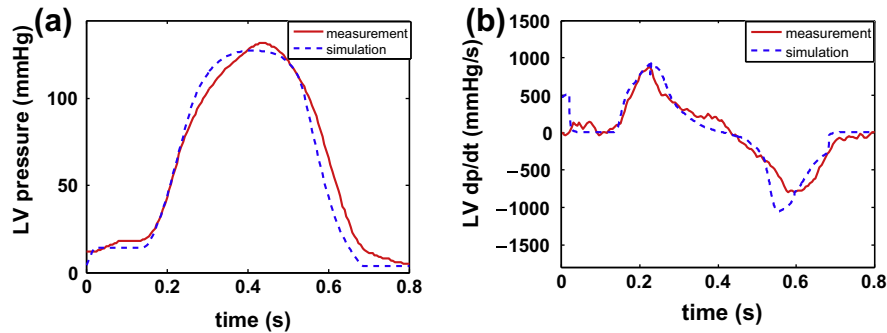
6.2. Model personalisation

We input into the model the depolarisation and repolarisation times estimated in Section 4, and now adjust the mechanical material parameters. Some valuable information on the spatial distribution of these may be obtained from clinical measurements such as late enhancement MRI, but the actual values of the perturbed parameters cannot be directly measured. The completely automated estimation of these parameters is still a scientific challenge, but we demonstrate here that an interactive calibration of the parameters based on global physiological indicators and cardiac motion can provide already satisfactory predictability in the direct simulation of the cardiac function.

For this simulation, image information was no longer used to constrain the motion, thus boundary conditions are especially important to achieve realistic motion. As can be seen in the cine-MRI sequences, there is an epicardium area near the apex on the

Fig. 12. Comparison between the motion from the personalised mechanical model and the personalised kinematic model in radial (left) and circumferential (right) directions, for three (basal, mid and apical) ventricular regions.

Fig. 13. Measured (solid red) and simulated (dashed blue) (a) pressure curves and (b) dP/dt curves in sinus rhythm. (For interpretation of the references to colour in this figure legend, the reader is referred to the web version of this article.)

inferior wall with small displacements, probably in relation with the attachment of the pericardium to the diaphragm. We modelled this physiological feature by prescribing some stiff viscoelastic support as boundary conditions in this area. Furthermore, we used soft viscoelastic support conditions on the valve annuli to model the truncated anatomy. The corresponding viscoelastic coefficients also required proper calibration with respect to the motion observed in image sequences.

The constitutive parameters have then been manually calibrated using the pressure–volume loop and the cine-MRI by means of the local motion pattern of the ventricles. In a nutshell, the hyperelastic constitutive parameters were calibrated using the data (ventricle pressure and volume) corresponding to the atrial contraction. Next, the tissue contractility was globally adjusted to obtain an adequate ejection fraction when maintaining a fixed value for the arterial pressure, namely, the measured end-systolic pressure. In order to represent the less contractile areas, the corresponding contractility parameters were weighted by a factor 1/5 with respect to their global value, as substantiated in Chabiniok et al. (2009). Finally, the Windkessel parameters (proximal capacitance C_p, resistance R_p, distal capacitance C_d and resistance R_d) were calibrated so as to obtain an adequate arterial pressure curve over the whole cycle.

6.3. Error analysis

With these personalised parameters, we obtain a simulated motion relatively close to the one estimated from the personalised

kinematics. We compared the simulated motion with the personalised mechanical parameters to the motion extracted from the images with the personalised kinematic model and we obtained differences close to the in-plane voxel size (see Fig. 12).
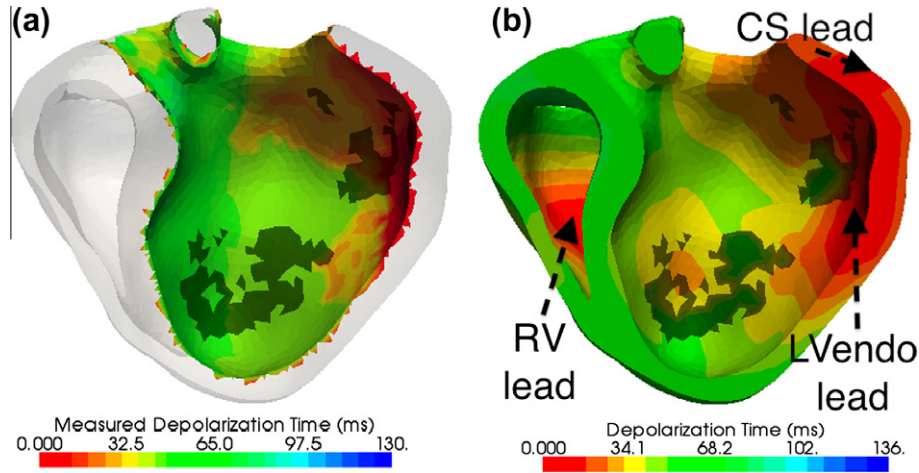
We output the simulated ventricular pressure and compared it with the measurements, see Fig. 13. This personalised mechanical model simulated a ventricular pressure curve in very good agreement with the catheter measurement (see Fig. 13).

From this interactive adjustment, it was observed that for these two patients, the global contractility was a key parameter in the pressure personalisation, and the local adjustments were mostly correcting the differences in local motion, without much impact on the global indices.
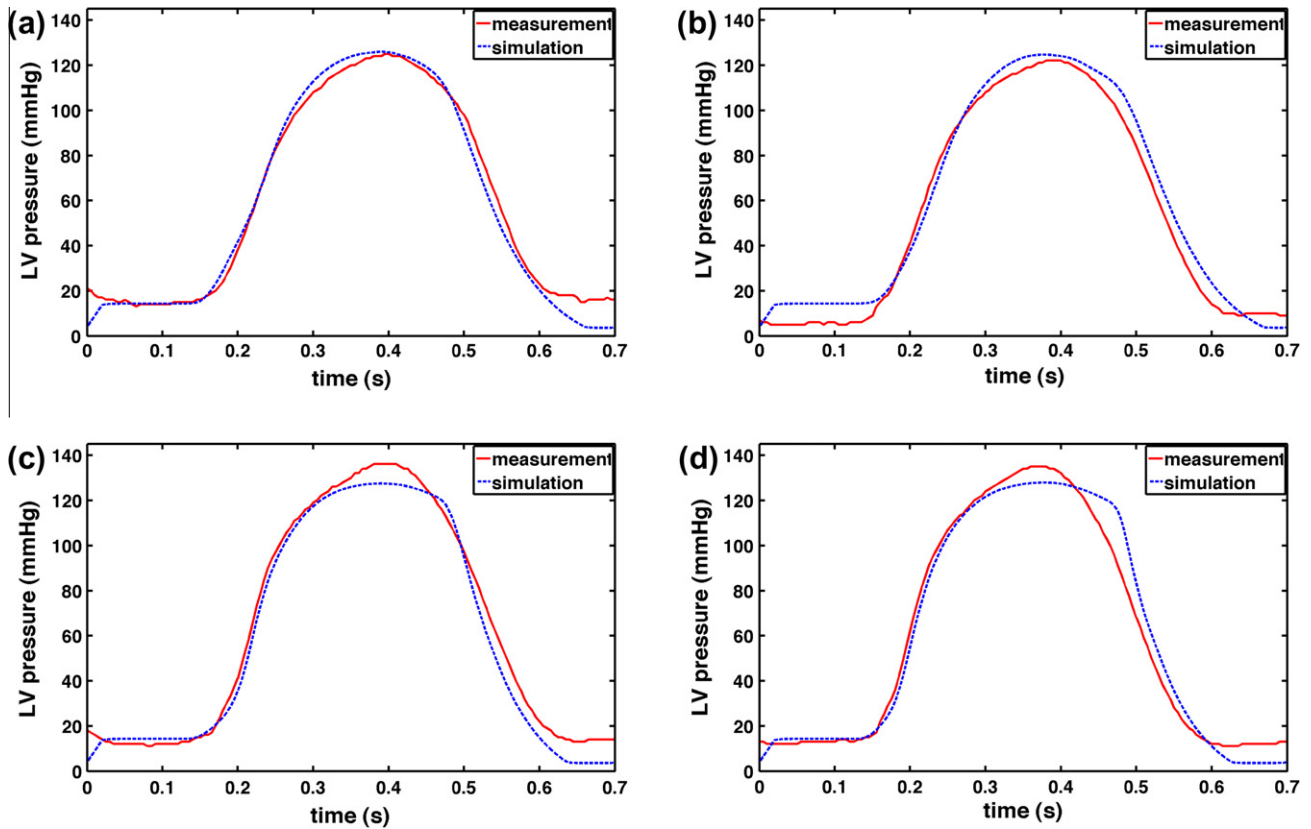
Note that the slope of the simulated pressure curve (dP/dt) is less accurate in the diastolic phase as the repolarisation time measurement from non-contact mapping data is more difficult due to the small size of the T wave and far-field effects, but CRT mostly focus on the contraction phase.

7. Prediction of the acute effects of pacing on LV pressure

During the acute electrophysiological study preceding device implantation, different pacing configurations were tested to evaluate the effect of different lead locations and delays. We measured the acute haemodynamic response to different pacing parameters and lead locations. This was assessed using a pressure wire in

Fig. 14. (a) Measured isochrones for TriV pacing, projected on the MR endocardium. The onsets on the LV free wall from the coronary sinus (CS) and endocardial (LVendo) pacing catheters are clearly visible. (b) Predicted volumetric isochrones using the AC map estimation from the known onset locations in LV and RV and the endocardial activation.

Fig. 15. Measured (solid red) and predicted (dashed blue) pressure curves for (a) atrial, (b) RV, (c) LVendo, and (d) TriV pacing modes. (For interpretation of the references to colour in this figure legend, the reader is referred to the web version of this article.)

the LV cavity from which we were able to measure dP/dt. This also provides the opportunity to estimate what could be the expected haemodynamic benefit from the pacemaker implant.
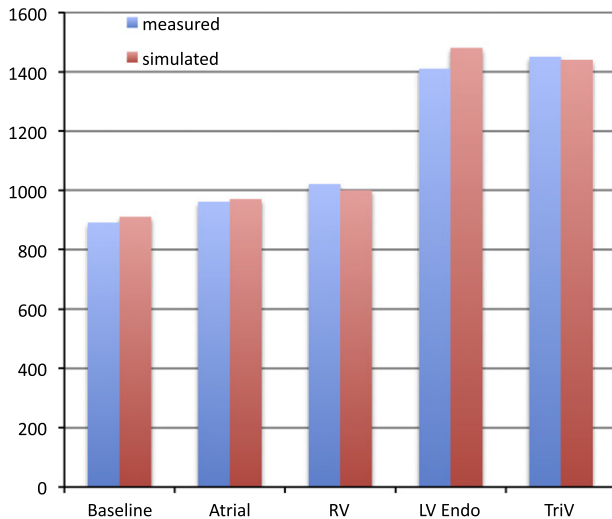
In this section, we tested the ability of our personalised electromechanical model of the myocardium to predict the changes in the heart function due to a new pacing condition. The different pacing protocols tested here were atrial pacing (atrial), right ventricular pacing (RV), left ventricular endocardial pacing (LVendo), biventricular pacing (BiVsim), and biventricular pacing with simultaneous endocardial left ventricular pacing (TriV). We first estimated the

volumetric depolarisation isochrones using the method of Section 4 and then input these isochrones into the already personalised model of Section 6 to simulate the new pressure curve.

For each of the pacing modes, we used the personalisation strategy of Section 4 to obtain the volumetric depolarisation isochrones from the endocardial mapping data. The obtained endocardial isochrones are in good agreement with the data (see for instance Fig. 14b).

Over all the different pacing modes and regions, we obtained an average AC of 1.68 ± 0.29 for Patient 1 and 2.74 ± 0.61 for Patient 2.
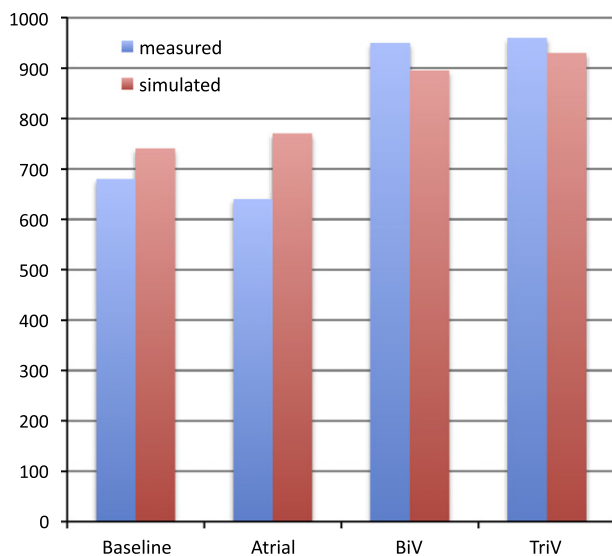
Fig. 16. Patient 1: Measured (blue) and simulated (red) $(dP/dt)_{max}$ for different pacing conditions. Parameters were estimated on baseline and then kept constant. (For interpretation of the references to colour in this figure legend, the reader is referred to the web version of this article.)

Fig. 17. Patient 2: Measured (blue) and simulated (red) $(dP/dt)_{max}$ for different pacing conditions. Parameters were estimated on baseline and then kept constants. (For interpretation of the references to colour in this figure legend, the reader is referred to the web version of this article.)

Each pacing configuration was producing AC maps with the same global characteristics, but local modifications fitting the local specificities of each pacing helped in achieving a good accuracy in all the cases.

For the mechanical predictions, we used the model personalised in Section 6 on baseline in sinus rhythm, without changing any parameter, including the Windkessel parameters. To achieve these mechanical model predictions, we only input the new electrical command corresponding to the different pacing conditions. Hence, the model parameters were not changed, except for the electrical activation input.

7.1. Model predictions

The resulting simulated pressure curves (see Fig. 15) obtained are in very good agreement with the measured. These curves al-

Table 4
Patient 1 measured and simulated dP/dt_{max} in mm Hg s^{-1}.

Pacing	Measured	Simulated
Baseline	890	930
Atrial	960	970
RV	1020	1000
LV endo	1410	1440
TriV	1450	1420

Table 5
Patient 2 measured and simulated dP/dt_{max} in mm Hg s^{-1}.

Pacing	Measured	Simulated
Baseline	680	740
Atrial	640	770
BiV	950	895
TriV	960	930

lowed to test in particular the predictions on the slope changes of this pressure, which is sought to be optimised by CRT. One important index of the effectiveness of the contraction is the maximum of the pressure time-derivative, $(dP/dt)_{max}$. It describes how the pressure builds up during the isovolumetric contraction. We present in Figs. 16 and 17 the results on the predictions of $(dP/dt)_{max}$ for the two patients (numerical figures can be found in Tables 4 and 5).

7.2. Error analysis

For this first patient, the different simulated pacing modes with the model personalised from baseline measurements achieved a very good agreement of the predicted pressure curve with the recorded data from the pressure catheter (see Fig. 15a). The improvement of the cardiac function brought by the pacing in Patient 1 was very reliably predicted by the *in silico* simulations. Such accuracy was achieved for all the different pacing modes (see Fig. 16).

We applied exactly the same methodology on Patient 2, with a more pronounced dilated cardiomyopathy (DCM) and without any myocardial scar. A functional conduction block was visible from the electrophysiological mapping data, which was reproduced in the personalised model. For the mechanical personalisation, in order to achieve a good adjustment to the measured motion and pressure, the passive tissue stiffness was increased (see Table 3). This could be explained by a fibrotic remodelling in a highly developed DCM. The adjustment on baseline and the predictions of $(dP/dt)_{max}$ for atrial, BiV, and TriV pacing are presented in Fig. 17.

For this second patient, the predictions were still in agreement with the measurements, however with a slightly larger error. This is probably due to the influence of functional block in viable tissue and therefore a binary definition of block and healthy tissue may be too simplistic since the conduction properties are more heterogeneous than the current modelling parameters allow. Moreover, the transmurality of such block is harder to evaluate as it does not appear in images. The adjustment of the electrophysiology model was more difficult, which can explain the loss in accuracy of the resulting mechanical simulations.

Overall, in these two patients we obtained a mean error on simulated dP/dt_{max} of 47.5 ± 35 mm Hg s^{-1}, which is less than 5% error. This is a very low error, given the different potential sources of error in this whole personalisation.

8. Discussion

We obtained promising results using models that are tractable in terms of complexity and observability. Such mechanical predic-

tions are in themselves already an interesting result in order to evaluate the relevance of such models. But in addition to the different sources of error that are listed in the "Error Analysis" paragraph of each personalisation section, there are different limitations to the current method:

Anatomical personalisation. The automatic extraction of the different structures of the heart from medical images is now becoming available (Ecabert et al., 2008; Zheng et al., 2008; Peters et al., 2010). Regarding the fibre orientation, it is known that scarring affects local fibre organisation (Zimmerman et al., 2000), but this is not incorporated into in our anatomical model at present. As conductivity and contractility are reduced within the scars in the simulations, the impact of these organisational changes may be limited. Recent progress with *in vivo* cardiac DTI are very encouraging for patient-specific fibre architecture measurement (Wu et al., 2009; Toussaint et al., 2010) and could be used instead of the currently prescribed directions. However, data on the myocyte layers will be significantly harder to measure, thus the effects of the orthotropic anisotropy would only come from prior knowledge (Caldwell et al., 2009).

Electrophysiology predictions. The accuracy of the final predictions in the different pacing modes relies heavily on the accuracy of the volumetric isochrones provided to the mechanical model. We preferred here to separate the mechanical predictions from the electrophysiological predictions of the model, because with this clinical setting, a reliable estimation of the volumetric conductivity is difficult. Challenges come from the acquisition device (non-contact mapping catheter relying on an inverse problem), the surface reconstruction from a roving catheter for this inverse problem, the registration between this surface and the imaging data, and the only partial observation on the endocardium that we have to extrapolate to the whole myocardium.

Mechanical personalisation. Another limitation is the manual adjustment of the mechanical parameters. The methodology for automatic parameter estimation is becoming available (Sermesant et al., 2006b; Moreau et al., 2008; Wang et al., 2009; Moreau et al., 2009). Any available motion information (for instance from tagged-MRI) can be directly used within such frameworks. A robust method for automatic mechanical parameter estimation from patient data would make the translation of such methods into clinical practice achievable. But the small deformation observed in such heart failure patients makes their clinical application challenging.

Invasiveness of the data. We tested here the models on rich and invasive data, but in order to be more clinically useful the final aim is to obtain similar results from less invasive data. For instance, the sinus rhythm activation map could be obtained from body surface potential mapping, see e.g. (Pfeifer et al., 2008). If we can validate the personalisation and the predictions of the electrophysiology model from such data, it would be a great step towards a non-invasive approach.

Data and model uncertainties. There are still important challenges in order to tackle personalisation robustly. One of the main difficulties is to be able to include uncertainty on the data and the model. Modern approaches (e.g. integrating polynomial chaos and compressed sensing) offer new ways to handle this explicitly in a tractable manner, as in Konukoglu et al. (2011).

9. Conclusion and perspectives

We have developed and demonstrated a personalised electromechanical modelling technique to determine patient-specific estimates of myocardial conductivity and contractility parameters using cardiac MRI, LV endocardial electrophysiological mapping and pressure recordings. We then used this model to predict the acute haemodynamic effects of different left ventricular pacing configurations in two subjects with heart failure. The behaviour of the model in sinus rhythm as well as the predictions of the model under different pacing conditions compare well with the measured data for these two clinical cases, which makes such an approach very promising.

This case study demonstrated how electromechanical models of the heart can be adjusted to be patient-specific and is a first validation of how this approach may be useful for therapy planning. By integrating information about the anatomy, the electrophysiology, the kinematics and the mechanics, we can explore the correlation between these different aspects for a given patient in order to provide an integrated view of the patient's cardiac function and simulate and evaluate different therapies before their actual application.

This method is still a relatively complex pipeline, however there are interesting perspectives in order to automate many steps and simplify its application. When validated, our method can provide a way to test the effects of pacing before the actual implant and optimise the pacing leads positions and delays based on *in silico* tests to improve the clinical response to CRT in individual patients. Such a model-based approach is promising for therapies like CRT that are complex to explore and optimise. They can help in building new clinical indexes and biomarkers in order to better plan and evaluate therapy. However there is an important need for uncertainty quantification in these approaches, in order to be able to estimate a confidence level on the predictions.

Acknowledgements

References

Aggarwal, N.R., Martinez, M.W., Gersh, B.J., Chareonthaitawee, P., 2009. Role of cardiac MRI and nuclear imaging in cardiac resynchronization therapy. Nature Reviews Cardiology 6, 759–770.

Beeler, G.W., Reuter, H., 1977. Reconstruction of the action potential of ventricular myocardial fibers. Journal of Physiology 268, 177–210.

Beshai, J.F., Grimm, R.A., Nagueh, S.F., Baker, J.H., Beau, S.L., Greenberg, S.M., Pires, L.A., Tchou, P.J., 2007. Cardiac-resynchronization therapy in heart failure with narrow QRS complexes. New England Journal of Medicine 357, 2461–2471.

Bestel, J., Clément, F., Sorine, M., 2001. A biomechanical model of muscle contraction. In: Niessen, W., Viergever, M. (Eds.), Medical Image Computing and Computer-Assisted intervention (MICCAI'01). Springer-Verlag, Berlin, Germany, pp. 1159–1161.

Billet, F., Sermesant, M., Delingette, H., Ayache, N., 2008. Cardiac motion recovery by coupling an electromechanical model and Cine-MRI data: first steps. In: Workshop Computational Biomechanics for Medicine III (MICCAI'08).

Billet, F., Sermesant, M., Delingette, H., Ayache, N., 2009. Cardiac motion recovery and boundary conditions estimation by coupling an electromechanical model and cine-MRI data. In: Proceedings of Functional Imaging and Modeling of the Heart 2009 (FIMH'09), pp. 376–385.

Caillerie, D., Mourad, A., Raoult, A., 2003. Cell-to-muscle homogenization: application to a constitutive law for the myocardium. Mathematical Modelling and Numererical Analysis 37, 681–698.

Caldwell, B.J., Trew, M.L., Sands, G.B., Hooks, D.A., LeGrice, I.J., Smaill, B.H., 2009. Three distinct directions of intramural activation reveal nonuniform side-to-side electrical coupling of ventricular myocytes. Circulation Arrhythmia Electrophysiology 2, 433–440.

Cazeau, S., Leclercq, C., Lavergne, T., Walker, S., Varma, C., Linde, C., Garrigue, S., Kappenberger, L., Haywood, G.A., Santini, M., Bailleul, C., Daubert, J.C., 2001. Multisite stimulation in cardiomyopathies (MUSTIC) study investigators, effects of multisite biventricular pacing in patients with heart failure and intraventricular conduction delay. New England Journal of Medicine 344, 873–880.

Chabiniok, R., Chapelle, D., Lesault, P., Rahmouni, A., Deux, J., 2009. Validation of a biomechanical heart model using animal data with acute myocardial infarction. In: CI2BM09 – MICCAI Workshop on Cardiovascular Interventional Imaging and Biophysical Modelling, London, UK.

Chapelle, D., Clément, F., Génot, F., Tallec, P.L., Sorine, M., Urquiza, J., 2001. A physiologically-based model for the active cardiac muscle contraction. In:

Katila, Magnin, I., Clarysse, P., Montagnat, J., Nenonen, J. (Eds.), Functional Imaging and Modeling of the Heart (FIMH'01). Springer, pp. 128–133.

Chinchapatnam, P., Rhode, K., Ginks, M., Rinaldi, C., Lambiase, P., Razavi, R., Arridge, S., Sermesant, M., 2008. Model-based imaging of cardiac apparent conductivity and local conduction velocity for diagnosis and planning of therapy. IEEE Transactions on Medical Imaging 27, 1631–1642.

Chung, E.S., Leon, A.R., Tavazzi, L., Sun, J.P., Nihoyannopoulos, P., Merlino, J., Abraham, W.T., Ghio, S., Leclercq, C., Bax, J.J., Yu, C.M., Gorcsan, J., St John Sutton, M., De Sutter, J., Murillo, J., 2008. Results of the predictors of response to crt (PROSPECT) trial. Circulation 117, 2608–2616.

Cleland, J.G., Daubert, J.C., Erdmann, E., Freemantle, N., Gras, D., Kappenberger, L., Tavazzi, L., 2005. Cardiac resynchronization-heart failure (CARE-HF) study investigators, the effect of cardiac resynchronization on morbidity and mortality in heart failure. New England Journal of Medicine 352, 1539–1549.

Colli Franzone, P., Guerri, L., Rovida, S., 1990. Wavefront propagation in activation model of the anisotropic cardiac tissue: asymptotic analysis and numerical simulations. Journal of Mathematical Biology, 28.

Crampin, E.J., Halstead, M., Hunter, P., Nielsen, P., Noble, D., Smith, N., Tawhai, M., 2004. Computational physiology and the physiome project. Experimental Physiology 89, 1–26.

Ecabert, O., Peters, J., Schramm, H., Lorenz, C., von Berg, J., Walker, M.J., Vembar, M., Olszewski, M.E., Subramanyan, K., Lavi, G., Weese, J., 2008. Automatic model-based segmentation of the heart in CT images. IEEE Transactions on Medical Imaging 27, 1189–1201.

Hodgkin, A., Huxley, A., 1952. A quantitative description of membrane current and its application to conduction and excitation in nerve. Journal of Physiology 177, 500–544.

Hu, Z., Metaxas, D., Axel, L., 2003. In vivo strain and stress estimation of the heart left and right ventricles from MRI images. Medical Image Analysis 7, 435–444.

Humphrey, J., 2002. Cardiovascular Solid Mechanics. Springer.

Humphrey, J., Strumpf, R., Yin, F., 1990. Determination of a constitutive relation for passive myocardium: I. A new functional form. ASME Journal of Biomechanical Engineering 112, 333–339.

Hunter, P., McCulloch, A., ter Keurs, H., 1998. Modelling the mechanical properties of cardiac muscle. Progress in Biophysics & Molecular Biology 69, 289–331.

Hunter, P., Nash, M., Sands, G., 1997. Computational Biology of the Heart. Computational Electromechanics of the Heart. John Wiley & Sons Ltd, West Sussex UK, pp. 345–407, Chapter 12.

Hunter, P., Nielsen, P., 2005. A strategy for integrative computational physiology. Physiology (Bethesda) 20, 316–325.

Ismail, H., Makaryus, A.N., 2010. Predictors of response to cardiac resynchronization therapy: the holy grail of electrophysiology. International Journal of Cardiovascular Imaging 26, 197–198.

Keener, J., Sneyd, J., 1998. Mathematical Physiology. Springer.

Kerckhoffs, R.C., Lumens, J., Vernooy, K., Omens, J.H., Mulligan, L.J., Delhaas, T., Arts, T., McCulloch, A.D., Prinzen, F.W., 2008a. Cardiac resynchronization: Insight from experimental and computational models. Progress in Biophysics & Molecular Biology 97, 543–561.

Kerckhoffs, R.C., McCulloch, A.D., Omens, J.H., Mulligan, L.J., 2008b. Effects of biventricular pacing and scar size in a computational model of the failing heart with left bundle branch block. Medical Image Analysis.

Kerckhoffs, R.C., Narayan, S.M., Omens, J.H., Mulligan, L.J., McCulloch, A.D., 2008c. Computational modeling for bedside application. Heart Failure Clinics 4, 371–378.

Kerckhoffs, R.C., Omens, J.H., McCulloch, A.D., Mulligan, L.J., 2010. Ventricular dilation and electrical dyssynchrony synergistically increase regional mechanical nonuniformity but not mechanical dyssynchrony: a computational model. Circulation Heart Failure 3, 528–536.

Kirn, B., Jansen, A., Bracke, F., van Gelder, B., Arts, T., Prinzen, F.W., 2008. Mechanical discoordination rather than dyssynchrony predicts reverse remodeling upon cardiac resynchronization. American Journal of Physiology – Heart and Circulatory Physiology 295, 640–646.

Konukoglu, E., Relan, J., Cilingir, U., Menze, B., Chinchapatnam, P., Jadidi, A., Cochet, H., Hocini, M., Delingette, H., Jaïs, P., Haïssaguerre, M., Ayache, N., Sermesant, M., 2011. Efficient probabilistic model personalization integrating uncertainty on data and parameters: application to Eikonal-Diffusion models in cardiac electrophysiology. Progress in Biophysics and Molecular Biology, in press, doi:10.1016/j.pbiomolbio.2011.07.002.

Le Tallec, P., 1994. Numerical methods for nonlinear three-dimensional elasticity. In: Ciarlet, P., Lions, J.L. (Eds.), Handbook of Numerical Analysis, vol. 3. Elsevier.

Liu, H., Shi, P., 2007. State-space analysis of cardiac motion with biomechanical constraints. IEEE Transactions on Image Processing 16, 901–917.

Luo, C., Rudy, Y., 1991. A model of the ventricular cardiac action potential: depolarization, repolarization, and their interaction. Circulation Research 68, 1501–1526.

McInerney, T., Terzopoulos, D., 1996. Deformable models in medical images analysis: a survey. Medical Image Analysis 1, 91–108.

Moireau, P., Chapelle, D., Le Tallec, P., 2008. Joint state and parameter estimation for distributed mechanical systems. Computer Methods in Applied Mechanics and Engineering 197, 659–677.

Moireau, P., Chapelle, D., Le Tallec, P., 2009. Filtering for distributed mechanical systems using position measurements: perspectives in medical imaging. Inverse Problems 25, 10–35.

Montagnat, J., Delingette, H., 2005. 4D deformable models with temporal constraints: application to 4D cardiac image segmentation. Medical Image Analysis 9, 87–100.

Moreau-Villéger, V., Delingette, H., Sermesant, M., Ashikaga, H., McVeigh, E., Ayache, N., 2006. Building maps of local apparent conductivity of the epicardium with a 2D electrophysiological model of the heart. IEEE Transactions on Biomedical Engineering 53, 1457–1466.

Nash, M., 1998. Mechanics and material properties of the heart using an anatomically accurate mathematical model. Ph.D. thesis, University of Auckland.

Noble, D., 1962. A modification of the Hodgkin–Huxley equations applicable to Purkinje fibre action and pace-maker potentials. Journal of Physiology 160, 317–352.

Noble, D., Varghese, A., Kohl, P., Noble, P., 1998. Improved guinea-pig ventricular cell model incorporating a diadic space, I_{Kr} and I_{Ks}, and length and tension dependent processes. Canadian Journal of Cardiology 14, 123–134.

Ourselin, S., Roche, A., Prima, S., Ayache, N., 2000. Block matching: a general framework to improve robustness of rigid registration of medical images. In: DiGioia, A., Delp, S. (Eds.), Third International Conference on Medical Robotics, Imaging And Computer Assisted Surgery (MICCAI 2000). Springer, Pittsburgh, Penn, USA, pp. 557–566.

Park, J., Metaxas, D., Axel, L., 1996. Analysis of left ventricular wall motion based on volumetric deformable models and MRI-SPAMM. Medical Image Analysis, 53–71.

Peters, J., Ecabert, O., Meyer, C., Kneser, R., Weese, J., 2010. Optimizing boundary detection via simulated search with applications to multi-modal heart segmentation. Medical Image Analysis 14, 70–84.

Peyrat, J.M., Sermesant, M., Pennec, X., Delingette, H., Xu, C., McVeigh, E.R., Ayache, N., 2007. A computational framework for the statistical analysis of cardiac diffusion tensors: application to a small database of canine hearts. IEEE Transactions on Medical Imaging 26, 1500–1514.

Pfeifer, B., Hanser, F., Seger, M., Fischer, G., Modre-Osprian, R., Tilg, B., 2008. Patient-specific volume conductor modeling for non-invasive imaging of cardiac electrophysiology. Open Medical Informatics Journal 2, 32–41.

Powell, M., 2006. The NEWUOA software for unconstrained optimization without derivatives. In: Pillo, G.D., Roma, M. (Eds.), Large-Scale Nonlinear Optimization. Springer, pp. 255–297.

Rhode, K., Sermesant, M., Brogan, D., Hegde, S., Hipwell, J., Lambiase, P., Rosenthal, E., Bucknall, C., Qureshi, S., Gill, J., Razavi, R., Hill, D., 2005. A system for real-time XMR guided cardiovascular intervention. IEEE Transactions on Medical Imaging 24, 1428–1440.

Sachse, F.B., 2004. In: Computational Cardiology, Modeling of Anatomy, Electrophysiology, and Mechanics. Lecture Notes in Computer Science, vol. 2966. Springer.

Sainte-Marie, J., Chapelle, D., Cimrman, R., Sorine, M., 2006. Modeling and estimation of the cardiac electromechanical activity. Computers & Structures 84, 1743–1759.

Sermesant, M., Delingette, H., Ayache, N., 2006a. An electromechanical model of the heart for image analysis and simulation. IEEE Transactions in Medical Imaging 25, 612–625.

Sermesant, M., Konukoglu, E., Delingette, H., Coudiere, Y., Chinchaptanam, P., Rhode, K., Razavi, R., Ayache, N., 2007. An anisotropic multi-front fast marching method for real-time simulation of cardiac electrophysiology. In: Proceedings of Functional Imaging and Modeling of the Heart 2007 (FIMH'07), pp. 160–169.

Sermesant, M., Moireau, P., Camara, O., Sainte-Marie, J., Andriantsimiavona, R., Cimrman, R., Hill, D.L., Chapelle, D., Razavi, R., 2006b. Cardiac function estimation from MRI using a heart model and data assimilation: advances and difficulties. Medical Image Analysis 10, 642–656.

Smith, N., Nickerson, D., Crampin, E., Hunter, P., 2000. Computational mechanics of the heart: from tissue structure to ventricular function. Journal of Elasticity 61, 113–141.

Stergiopulos, N., Westerhof, B., Westerhof, N., 1999. Total arterial inertance as the fourth element of the windkessel model. American Journal of Physiology 276, H81–H88.

Streeter, D., 1979. Handbook of Physiology. Williams & Wilkins, Chapter: The Cardiovascular System: Gross Morphology and Fiber Geometry of the Heart.

Sutton, M.S., Keane, M.G., 2007. Reverse remodelling in heart failure with cardiac resynchronisation therapy. Heart 93, 167–171.

Ten Tusscher, K., Noble, D., Noble, P., Panfilov, A., 2004. A model of the human ventricular myocyte. American Journal of Physiology – Heart and Circulatory Physiology 286, 1573–1589.

Tomlinson, K., 2000. Finite element solution of an eikonal equation for excitation wavefront propagation in ventricular myocardium. Ph.D. thesis, University of Auckland.

Toussaint, N., Mansi, T., Delingette, H., Ayache, N., Sermesant, M., 2008. An integrated platform for dynamic cardiac simulation and image processing: application to personalised tetralogy of fallot simulation. In: Proceedings of Eurographics Workshop on Visual Computing for Biomedicine (VCBM), Delft, The Netherlands.

Toussaint, N., Stoeck, C., Sermesant, M., Kozerke, S., Batchelor, P., 2010. Three-dimensional prolate spheroidal extrapolation for sparse DTI of the in-vivo heart. In: International Society for Magnetic Resonance in Medicine (ISMRM) Scientific Meeting.

Turk, G., O'Brien, J., 1999. Variational implicit surfaces. Technical report, Georgia Institute of Technology.

Wang, V.Y., Lam, H.I., Ennis, D.B., Cowan, B.R., Young, A.A., Nash, M.P., 2009. Modelling passive diastolic mechanics with quantitative MRI of cardiac structure and function. Medical Image Analysis 13, 773–784.

Wong, K., Billet, F., Mansi, T., Chabiniok, R., Sermesant, M., Delingette, H., Ayache, N., 2010. Cardiac motion estimation using a proactive deformable model: evaluation and sensitivity analysis. In: Camara, O., Pop, M., Rhode, K., Sermesant, M., Smith, N., Young, A. (Eds.), Statistical Atlases and Computational Models of the Heart. Springer, Berlin/Heidelberg, pp. 154–163.

Wu, M.T., Su, M.Y., Huang, Y.L., Chiou, K.R., Yang, P., Pan, H.B., Reese, T.G., Wedeen, V.J., Tseng, W.Y., 2009. Sequential changes of myocardial microstructure in patients postmyocardial infarction by diffusion-tensor cardiac MR: correlation with left ventricular structure and function. Circulation: Cardiovascular Imaging 2, 32–40.

Yan, P., Sinusas, A., Duncan, J.S., 2007. Boundary element method-based regularization for recovering of LV deformation. Medical Image Analysis 11, 540–554.

Zheng, Y., Barbu, A., Georgescu, B., Scheuering, M., Comaniciu, D., 2008. Four-chamber heart modeling and automatic segmentation for 3-D cardiac CT volumes using marginal space learning and steerable features. IEEE Transactions on Medical Imaging 27, 1668–1681.

Zimmerman, S.D., Karlon, W.J., Holmes, J.W., Omens, J.H., Covell, J.W., 2000. Structural and mechanical factors influencing infarct scar collagen organization. American Journal of Physiology – Heart and Circulatory Physiology 278, 194–200.